CHINA FOUNDRY Research & Development
Vol. 22 No. 5 September 2025
www.springer.com/41230
https://doi.org/10.1007/s41230-025-5001-5

Mitigating anisotropy of vat photopolymerization 3D printing Al_2O_3-based ceramic cores through zircon addition

Bo-yang Qu[1, 3], Rui-long Yu[2], Tian-chi Chen[1], *Qiao-lei Li[1], Ang Li[4], Wei Liu[4, 5, 6], Xi-he Liu[4], Xin-yan Yue[3, 7], Jing-jing Liang[1, 8], and **Jin-guo Li[1, 8]

1. *Shi-changxu Innovation Center for Advanced Materials, Institute of Metal Research, Chinese Academy of Sciences, Shenyang 110016, China*
2. *State Key Laboratory of Advanced Casting Technologies, Shenyang 110022, China*
3. *Key Laboratory for Anisotropy and Texture of Materials (Ministry of Education), School of Materials Science and Engineering, Northeastern University, Shenyang 110819, China*
4. *China United Gas Turbine Technology Co., Ltd., Beijing 100016, China*
5. *School of Intelligence Science and Technology, University of Science and Technology Beijing, Beijing 100083, China*
6. *Beijing Advanced Innovation Center for Materials Genome Engineering, University of Science and Technology Beijing, Beijing 100083, China*
7. *Institute of Advanced Ceramics, School of Materials Science and Engineering, Northeastern University, Shenyang 110819, China*
8. *Space Manufacturing Technology (CAS Key Lab), Beijing 100094, China*

Abstract: Ceramic cores are important in the fabrication of superalloy hollow blades, which are increasingly characterized by intricate internal cavity channels. This complexity poses significant challenges to traditional manufacturing processes. The vat photopolymerization 3D printing technology provides a new choice for ceramic cores with complex structures. However, the lamellar structure of the vat photopolymerization 3D printed ceramic cores leads to the anisotropy. Meanwhile, the low strength and high shrinkage of ceramic cores restrict their industrial application. In this study, using Al_2O_3 powder as the main material, the effects of zircon content on the sintering shrinkage, open porosity, flexural strength, and other properties of Al_2O_3-based ceramic cores were studied to address the aforementioned issues. The influencing mechanism of zircon distribution on sintering shrinkage was analyzed, and the strengthening mechanism of mullite on ceramic cores was discussed from both thermodynamics and dynamics aspects. Through the comprehensive evaluation of ceramic core properties, the Al_2O_3-based ceramic core with 15vol.% zircon exhibits the optimal performance. Compared with the core samples without zirconium addition, the flexural strength of the Al_2O_3-based ceramic core with 15vol.% zircon increases from 14.80 MPa to 61.54 MPa at 25 °C, an increase of 315.8%; and from 4.91 MPa to 11.59 MPa at 1,500 °C, an increase of 136.0%. The shrinkage in the *Z*-axis is reduced by 21%, which better weakens the anisotropy of the shrinkage of 3D printed Al_2O_3-based ceramic cores. ZrO_2 phase and mullite phase are formed by zircon, which improve the comprehensive properties of Al_2O_3-based ceramic cores. The successful 3D printing of high-performance Al_2O_3-based ceramic cores via vat photopolymerization has promoted its industrial application for fabricating ceramic cores with complex structures.

Keywords: 3D printing; anisotropy; ceramic cores; flexural strength; sintering shrinkage

CLC numbers: TG221 Document code: A Article ID: 1672-6421(2025)05-592-11

1 Introduction

Hollow turbine blade is the key component of aeroengine[1-3], which has he complex inneral cooling channels to improve high temperature resistance[4,5]. The intricate cooling channels within hollow blades are fabricated using ceramic cores through precision casting[6-9]. Due to the high production efficiency, hot injection is widely used to prepare ceramic cores, which faces the challenge of preparing complex-

***Qiao-lei Li**

Male, Ph. D., Assistant Researcher. His research interests mainly focus on additive manufacturing of ceramics and precision casting of single crystal blades.

E-mail: qlli@imr.ac.cn

****Jin-guo Li**

Male, Ph. D., Researcher. His research interests mainly focus on precision casting of superalloys and additive manufacturing.

E-mail: jgli@imr.ac.cn

Authors Bo-yang Qu and Rui-long Yu contributed equally to this work.

Received: 2025-01-02; Revised: 2025-07-28; Accepted: 2025-09-18

structured ceramic cores[10-13]. The vat photopolymerization 3D printing solidifies the photosensitive resin layer by layer to obtain a solid model[14-16], which provides a new option for preparing complex-structured ceramic cores[17-20].

Ceramic cores usually include SiO_2-based ceramic cores and Al_2O_3-based ceramic cores. Al_2O_3-based ceramic core has excellent chemical stability and creep resistance, and its operating temperature is higher than that of SiO_2-based ceramic core[21]. Therefore, Al_2O_3-based ceramic cores are widely used in high-temperature casting of superalloy blades[22]. However, the very high chemical stability of Al_2O_3 poses challenges during the leaching process, making core removal difficult. To ensure the effective dissolution of the core after casting, the porosity of the Al_2O_3-based ceramic core should be greater than 20%. In addition, Al_2O_3-based ceramic cores require flexural strength greater than 20 MPa at 25 °C, and greater than 15 MPa at 1,500 °C[23]. The flexural strength and open porosity requirements are contradictory. The higher sintering temperatures improve the flexural strength but significantly reduce the porosity of the Al_2O_3-based ceramic cores. This limits its wider application prospects. Therefore, mineralizing agents are usually added to Al_2O_3-based ceramic cores to reduce sintering temperatures while improving the flexural strength and porosity[24]. The selection of mineralizer plays a decisive role in core shrinkage, deformation, and high temperature mechanical properties[25]. Zircon has excellent high temperature properties and chemical stability, which can hinder the flow of liquid phase and improve the creep resistance and high temperature properties of the cores. Therefore, zircon is often used as a mineralization agent for Al_2O_3-based ceramic cores.

The current research has improved the performance of 3D printed ceramic cores to a certain extent, but due to the step effects during the 3D printing process, the vat photopolymerization ceramic cores still have significant anisotropic problem in terms of sintering shrinkage, which is unfavorable to the casting process. Moreover, the comprehensive performance of vat photopolymerization ceramic cores still needs to be further improved. The shortcomings of sintering anisotropy and insufficient performance of Al_2O_3-based ceramic cores have restricted the wide application of vat photopolymerization 3D printing technology.

In this study, Al_2O_3-based ceramic samples with different zircon contents were prepared by vat photopolymerization 3D printing technology. The influencing mechanism of zircon addition on the anisotropy of sintering shrinkage, microstructure, and properties of vat photopolymerization 3D printed Al_2O_3-based ceramic cores was systematically studied. The results of the study will contribute to enhancing the application of Al_2O_3-based ceramic cores produced by vat photopolymerization 3D printing technology in the aerospace industry.

2 Experiment

2.1 Materials and preparation process

The preparation process of the ceramic samples included slurry preparation, vat photopolymerization molding, degreasing, and sintering. The ceramic slurry was composed of 55vol.% solid phase (ceramic powders) and 45vol.% liquid phase (photosensitive resins). The ceramic powder was composed of sieved Al_2O_3 (D_{50}=14.5 μm, Hecheng New Material Co., Ltd., China) and zircon (D_{50}=19.0 μm, Hecheng New Material Co., Ltd., China). Considering that the impurities in zircon may negative affect the sample performance, five compositions were designed: 0vol.%, 5vol.%, 10vol.%, 15vol.%, and 20vol.%. The liquid phase included TMPTA (Trimethylolpropane triacrylate, DSM-AGI), HDDA (1,6-Hexanedioldiacrylate, DSM-AGI), BASF 819 (Phenyl bis(2,4,6-trimethylbenzoyl)-phosphine oxide, BASF), and EFKA FA 4608 (BASF dispersant, BASF). The ceramic slurry was milled in a high-speed planetary ball mill at a speed of 400 rpm for 2 h (Changsha Mickey Instrument Equipment Co., Ltd., China). The diameter of the grinding ball was 10 mm, and the mass fraction ratio of the grinding ball to the ceramic slurry was 2:3. After vacuum defoaming, the ceramic slurry was printed by a vat photopolymerization 3D printer (Beijing TenDimensions Technology Co., Ltd., China) to obtain 40 mm×10 mm×4 mm ceramic green bodies. Figure 1 shows the preparation process of the Al_2O_3-based ceramic samples. The exposure time for each layer was 5 s, and the thickness of each layer was 100 μm, with a printing power

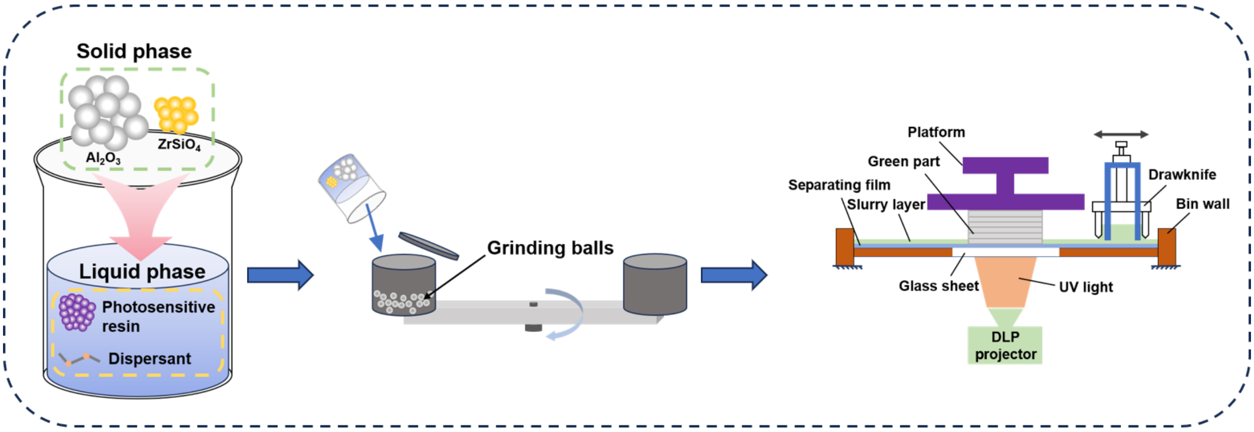

Fig. 1: Preparation process of Al_2O_3-based ceramic samples

of 3.56 mW·cm^{-2}. After the excess slurry on the surface was washed off, the green bodies were dried naturally in the shade. Finally, the green body was buried in 100 μm corundum sand. It was then subjected to degreasing at 500 °C for 1 h, followed by sintering at 1,400 °C for 6 h in air.

2.2 Performance testing

According to the size and weight change of ceramic samples before and after sintering, the shrinkage and weight loss rate of the ceramic samples were calculated. The calculation equations of sintering shrinkage and weight loss rate are as follows:

$$S = \frac{L_0 - L}{L_0} \times 100\% \tag{1}$$

$$M = \frac{m_0 - m}{m_0} \times 100\% \tag{2}$$

where S is the sintering shrinkage (%), L_0 is the length before sintering (mm), L is the length after sintering (mm), M is the weight loss rate (%), m_0 is the weight before sintering (g), and m is the weight after sintering (g).

The open porosity and bulk density of ceramic samples were measured by Archimedes drainage method. The calculation equations of bulk density (ρ) and porosity (W_a) are as follows:

$$\rho = \frac{m_1}{m_3 - m_2} \times \rho_{\text{water}} \times 100\% \tag{3}$$

$$W_a = \frac{m_3 - m_1}{m_3 - m_2} \times 100\% \tag{4}$$

where ρ is the bulk density (g·cm^{-3}), m_1 is the dry weight (g), m_2 is the floating weight (g), m_3 is the wet weight (g), and ρ_{water} is the density of the deionized water (g·cm^{-3}).

In order to simulate the service environment of ceramic cores, the tested ceramic samples were heated to high temperature of 1,500 °C and held for 30 min before flexural testing. Both room temperature (25 °C) strength and high temperature (1,500 °C) strength were tested by a high temperature flexural strength testing machine (HSST16-3000LX/W, Sinosteel Luoyang Institute of Refractories Research Co., Ltd.). The calculation equation of flexural strength (σ) is as follows:

$$\sigma = \frac{3PL_1}{2bh^2} \tag{5}$$

where σ is the flexural strength (MPa), P is the maximum load (N), L_1 is the length between the fulcrums (mm), b is the width of the samples (mm), and h is the height of the samples (mm).

2.3 Microstructure characterization

The fracture morphology and microstructure of the ceramic samples were characterized by a field emission scanning electron microscope (FE-SEM, FEI, Inspect F50, USA) equipped with an energy dispersive spectroscope (SEM-EDS). The phase constitution of ceramic samples with different zircon contents was characterized by an X-ray diffractometer (XRD, RIGAKU, SmartLab 9 kW, Japan). To further investigate the sintering behavior of the ceramic samples, the morphology and element distribution were characterized by a transmission electron microscope (TEM, JEOL, JEM-2100F, Japan) equipped with an energy dispersive spectroscope (TEM-EDS).

3 Results and discussion

3.1 Microstructure and phase constitution

Figures 2(a, b) show the SEM images of 3D printed Al_2O_3-based ceramic sample with 20vol.% zircon, where the distribution of zircon particles in the microstructure can be clearly observed. The 3D printed ceramic samples exhibit obvious lamellar structures and its thickness is slightly less than the set layer thickness. The anisotropic shrinkage along the three axes originates from the sintering-induced contraction of ceramic

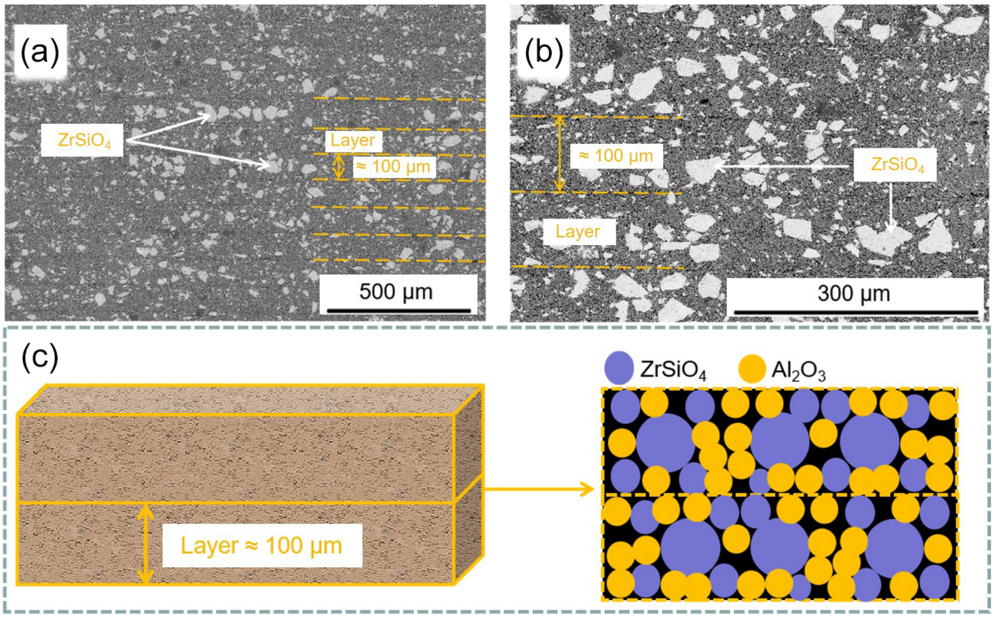

Fig. 2: Microstructure of Al_2O_3-based ceramic sample with 20vol.% zircon: (a, b) lamellar structure of ceramic samples; (c) schematic of the distribution of ceramic particles

particles and the non-uniform shrinkage of the layered structure[26]. Figure 2(c) shows the microscopic diagram of the layered structure of the 3D printed ceramic sample and the distribution law of the ceramic particles. The distribution of ceramic particles is affected by the size of powder. The large-size zircon particles are enriched in the middle of the lamella, while the small-size zircon and Al_2O_3 particles are mainly enriched at the interface of the lamella. The pores between the particles provide a channel for the resin to escape during the sintering process.

Figure 3 shows the SEM images of ceramic samples with different zircon contents. At the sintering temperature of 1,400 °C, zircon undergoes obvious decomposition phenomenon. Zircon distributes among Al_2O_3 particles and hinders the sintering of Al_2O_3 particles. With the increase of zircon content, the inhibiting effect on sintering becomes more obvious. As shown in Figs. 3(a, b), at a lower content of zircon, ZrO_2 is almost invisible. When the zircon content becomes high, the zircon particles decompose significantly, generating a large number of submicron ZrO_2 distributed around the Al_2O_3 particles, as shown in Figs. 3(c, d). With the decomposition of zircon, the formed SiO_2 promotes the sintering of Al_2O_3 particles and blocks some pores.

To analyze the decomposition behavior of zircon, the ceramic samples were further analyzed by EDS. Figure 4 shows the EDS images of the Al_2O_3 ceramic sample with 20vol.% zircon. Figure 4(a) shows that zircon with large particle size is embedded between Al_2O_3 particles. In Figs. 4(e, f), Si and Zr elements mostly coincide, and the excess Zr elements are scattered in surrounding areas, proving that ZrO_2 is dispersed within the materials and distributes among other ceramic particles in the form of submicron particles. This proves that the sintering temperature of 1,400 °C can meet the temperature conditions for the decomposition of zircon[27-29].

To further analyze the phase constitution of Al_2O_3-based ceramic samples with different zircon contents, the ceramic samples were tested by XRD, and the results are shown in Fig. 5. The phases in the patterns include Al_2O_3 (PDF#46-1212), ZrO_2 (PDF#79-1796) and $ZrSiO_4$ (PDF#80-1809). SiO_2 and mullite phases are not detected, which is not significantly correlated with the content of zircon. There are two reasons for why SiO_2 and mullite phase are not detected: (1) the

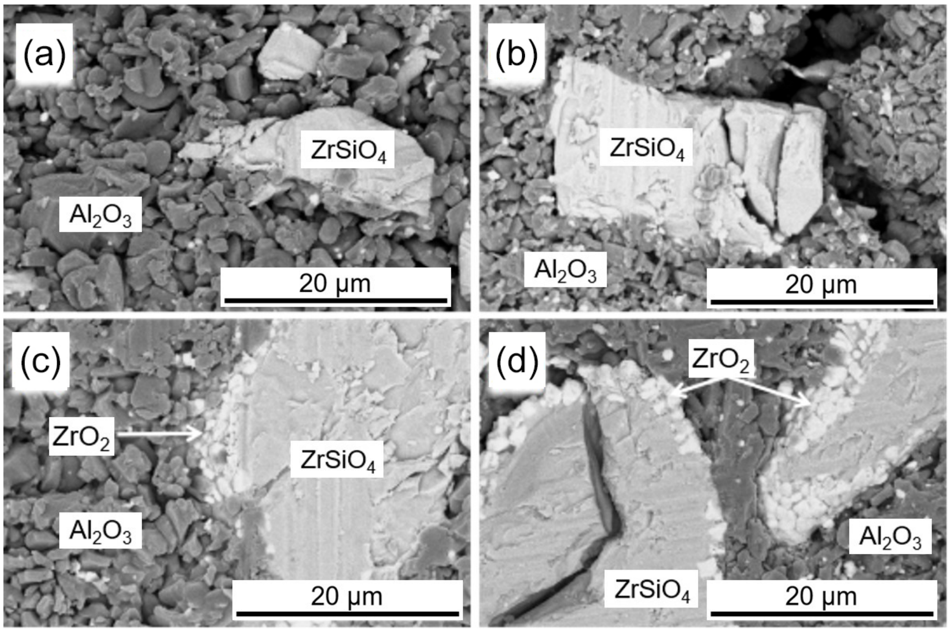

Fig. 3: Microstructure of Al_2O_3-based ceramic samples with different zircon contents: (a) 5vol.%; (b) 10vol.%; (c) 15vol.%; (d) 20vol.%

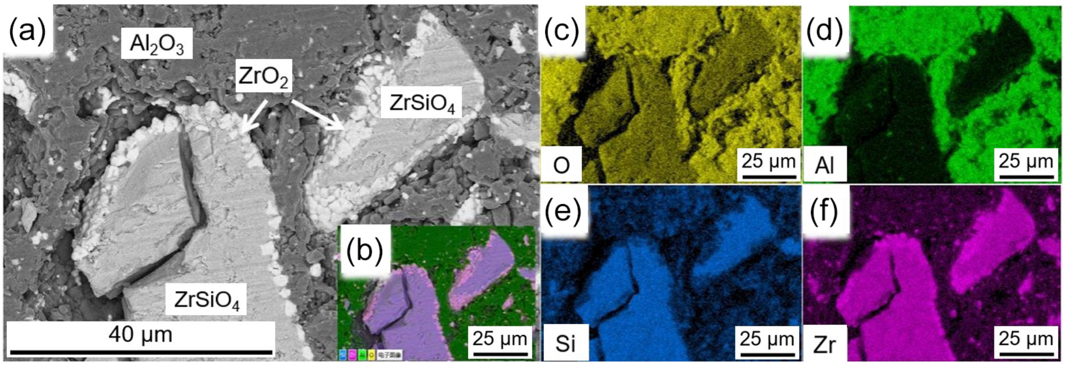

Fig. 4: EDS images of ceramic sample with 20vol.% zircon: (a) SEM image; (b–f) element distribution images

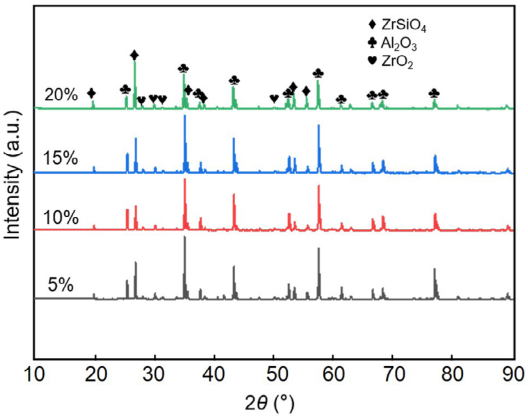

Fig. 5: XRD patterns of Al_2O_3-based ceramic samples with different zircon contents

decomposition of zircon results in a relatively low content of SiO_2, which leads to a smaller amount of mullite formation; (2) the intensity of Al_2O_3 phase is too high, covering up the low signal ceramic phase. Therefore, there are no SiO_2 and mullite phases in the XRD patterns.

3.2 Effect of zircon content on properties

Figure 6(a) shows the shrinkage of sintered Al_2O_3-based ceramic samples in different axes. With the increase of zircon content, the shrinkage along *X*-axis and *Y*-axis firstly decreases and then increases, but the variation fluctuation is generally stable within 2%. The formation of small particles causes an increase in the shrinkage of the *X* and *Y* axes. The shrinkage in *Z*-axis changes greatly and decreases with the increase of zircon content. With the increase of zircon content, the amount of SiO_2 and submicron ZrO_2 produced by zircon decomposition increases, which fills the pores of the ceramic particles. The shrinkage of *Z*-axis is significantly higher than that of the other two axes, which is resulted from the layer-by-layer forming of vat photopolymerization 3D printing in the direction of *Z*-axis[30]. Specifically, the small size zircon particles are distributed at the interface, and the ZrO_2 formed by zircon fills the interface particles of the core and hinders the sintering of the Al_2O_3 particles, thereby reducing the shrinkage of *Z*-axis with the increase of zircon content.

Figure 6(b) shows the weight loss rate of the sintered Al_2O_3-based ceramic samples. When the zircon content is 0vol.%, the weight loss rate of the ceramic samples is the largest, which is 19.13%. The weight loss rate of ceramic samples with zircon content of 5vol.%, 10vol.%, 15vol.%, and 20vol.% is 16.98%, 18.23%, 17.60%, and 16.57%, respectively. The disappearance of photosensitive resin is the main reason for the weight loss of ceramic core samples. During the sintering process, part of the Al_2O_3 sintered powder enters the pores or binds to the sample surface, leading to the existence of closed pores and impeding gas overflow, thus causing a small difference in the weight loss rate.

Figure 6(c) shows the open porosity and bulk density of Al_2O_3-based ceramic core samples with different zircon

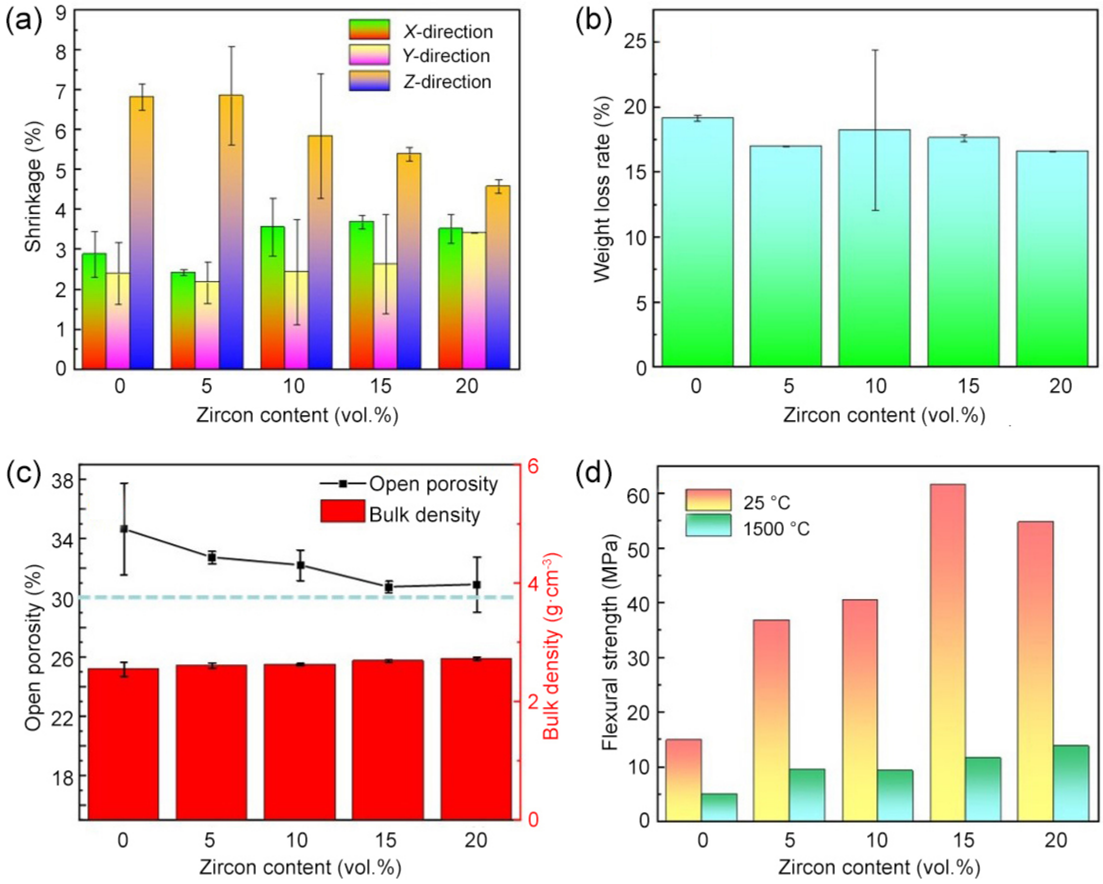

Fig. 6: Properties of Al_2O_3-based ceramic samples with different zircon contents: (a) shrinkage; (b) weight loss rate; (c) open porosity and bulk density; (d) flexural strength

contents. When the zircon content is less than 20vol.%, the porosity of the ceramic samples remains above 30%. The increase of zircon content reduces the porosity of Al_2O_3-based ceramic samples, which may be due to the fact that the submicron ZrO_2 generated by the decomposition of zircon fills part of the pores. At the same time, the pore is blocked by viscous flowing SiO_2 generated by zircon, which reduces the open porosity of Al_2O_3-based ceramic samples. As the zircon content increases to 20vol.%, the porosity of Al_2O_3-based ceramic samples decreases by less than 5%. When the sintering temperature is 1,400 °C, the zircon is partially decomposed, generated limited amounts of SiO_2 and submicron ZrO_2, thus, the sintering densification effect is not obvious[31]. When the sintering temperature is higher, the influence of zircon content on the porosity is more obvious[32]. In general, the bulk density is inversely proportional to the porosity. Figure 6(c) also shows that the bulk density gradually increases from 25.06 $g\cdot cm^{-3}$ to 25.89 $g\cdot cm^{-3}$ with the increase of zircon content from 0 to 20vol.%. When the zircon content is not more than 20vol.%, the porosity and bulk density of Al_2O_3-based ceramic samples meet the use requirements of ceramic cores[23].

Figure 6(d) shows the relationship between flexural strength and zircon content of Al_2O_3-based ceramic core samples at test temperature of 25 °C and 1,500 °C. When the zircon content increases from 0vol.% to 15vol.%, the flexural strength of Al_2O_3-based ceramic core samples increases sharply from 14.95 to 61.54 MPa at test temperature of 25 °C. When the zircon content is 20vol.%, the flexural strength of Al_2O_3 ceramic samples slightly reduces. With the increase of zircon content, the amount of submicron ZrO_2 and SiO_2 produced by zircon decomposition increases, which fills part of the pores, weakens the delamination phenomenon of the core, and gradually enhances the bending strength of the core. SiO_2 reacts with Al_2O_3 to form high-temperature stable mullite with fine crystal strengthening effect, reducing the adverse influence of SiO_2 on strength[33]. When increasing the zircon content to 20vol.%, the strong light-absorption of zircon leads to weakened interlayer bonding, resulting in a decrease in flexural strength at room temperature. Al_2O_3-based ceramic cores have low flexural strength at high temperatures because of low sintering temperatures[34,35], but they can still meet the requirements for core application.

3.3 Strengthening mechanism of zircon on structure

Figure 7 shows the TEM results of Al_2O_3 ceramic samples with 15vol.% zircon content. Figure 7(a) shows the high magnification TEM bright field image. The Si-rich region and Zr-rich region partially coincide with a size of about 1 μm, which indicates that the particle size of zircon decreases after sintering, but it is not completely decomposed. The Zr-rich area is distributed in a network, and the particle size of ZrO_2 generated by zircon decomposition is far less than 1 μm. ZrO_2 bonds to the surfaces of Al_2O_3 particles, and the nano-sized ZrO_2 forms an interconnected network that envelopes the Al_2O_3 particles. This enhances the bonding strength between the Al_2O_3 particles, increases the flexural strength of samples, and reduces their porosity. Combined with Figs. 7(b–d), it is found that a part of Al elements diffuses into SiO_2, reaching the mullite nucleation condition, and nano mullite is formed on the surface of Al_2O_3 particles [as shown by the red arrow in Fig. 7(a)]. The viscous flow of SiO_2 promotes the sintering among Al_2O_3 particles, zircon particles, and nano ZrO_2 particles, and therefore enhances the strength. The coincident of Al-rich area and Si-rich area in the vicinity of ZrO_2 proves

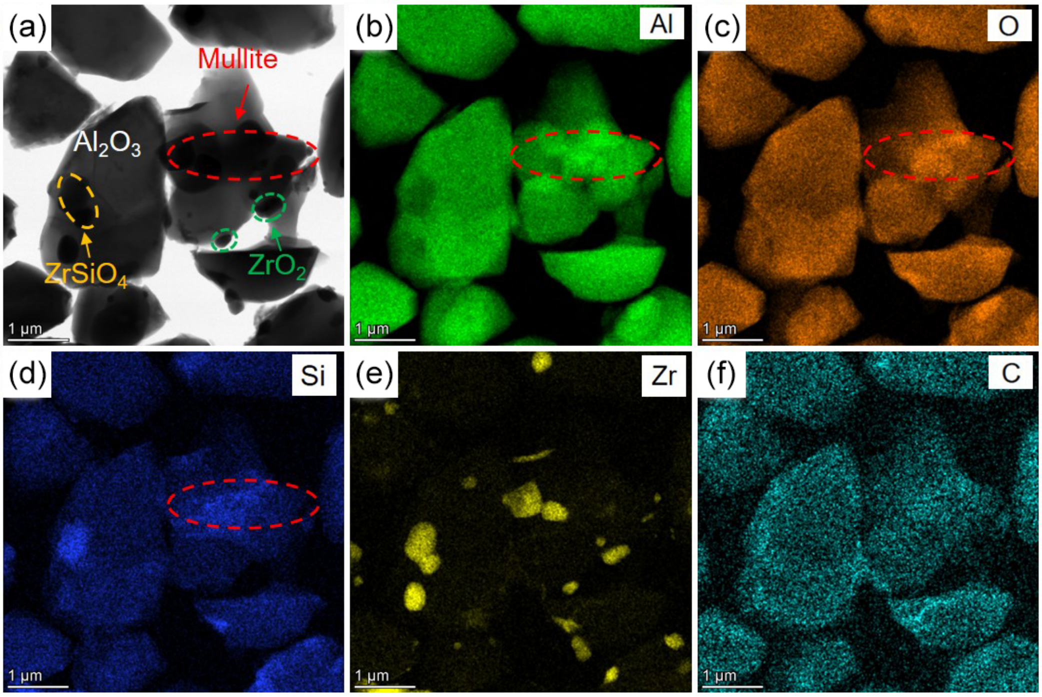

Fig. 7: TEM image (a) and element distribution images (b–f) of Al_2O_3-based ceramic sample with 15vol.% zircon

the interdiffusion of Al and Si ions. At the same time, it is proved that there is a prerequisite for the formation of mullite.

In the presence of impurities, the decomposition temperature of zircon can be reduced to about 1,200 °C[36]. At the sintering temperature of 1,400 °C, zircon decomposes into high activity SiO_2 and reacts with Al_2O_3 to form mullite. The chemical reaction equation is as follows:

$$ZrSiO_4 \rightarrow ZrO_2 + SiO_2 \quad (6)$$

$$3Al_2O_3 + 2SiO_2 \rightarrow 3Al_2O_3 \cdot 2SiO_2 \quad (7)$$

Combining Eq. (6) and Eq. (7), we can obtain:

$$3Al_2O_3 + 2ZrSiO_4 \rightarrow 3Al_2O_3 \cdot 2SiO_2 + 2ZrO_2 \quad (8)$$

According to Gibbs Helmholtz approximate equation[37]:

$$\Delta_r G_m^\theta = \Delta_r H_m^\theta - T \Delta_r S_m^\theta \quad (9)$$

where $\Delta_r G_m^\theta$ is the standard Gibbs free energy of the substance ($kJ \cdot mol^{-1}$), $\Delta_r H_m^\theta$ is the standard enthalpy of the formation of the substance ($kJ \cdot mol^{-1}$), $\Delta_r S_m^\theta$ is the standard entropy of matter [$J \cdot (mol \cdot K)^{-1}$], and T is the temperature (K). It is calculated that mullite can be generated spontaneously at 1,700 K (1,427 °C). However, the actual formation temperature is lower than the theoretical formation temperature.

Robie[38] pointed out that the free energy of $ZrSiO_4/Al_2O_3$ reaction can be expressed by the linear equation of temperature:

$$\Delta_r G_m^\theta = 72.19 - 0.0515T \quad (10)$$

It is concluded that mullite can be formed by reaction at a temperature greater than 1,400 K (1,127 °C). The linear equation of free energy of $ZrSiO_4/Al_2O_3$ reaction given by Li[39] is:

$$\Delta_r G_m^\theta = 73.75 - 0.05375T \quad (11)$$

It is concluded that mullite can be formed when the temperature is greater than 1,372 K (1,099 °C). The variation in the formation temperature of mullite reported by different authors can be attributed to differences in the impurity content of raw materials. These impurities play a significant role in influencing the decomposition of zircon and the subsequent formation of mullite. In this study, both the decomposition temperature of zircon and the formation temperature of mullite have been reduced to below 1,400 °C due to the presence of impurities. Additionally, the particle sizes of the zircon powder and Al_2O_3 powder differ significantly. The particle size of zircon has a direct effect on the degree of decomposition[40]. The relationship between reaction rate constant (k) and radius (r) is:

$$k = \alpha / r^2 \quad (12)$$

where α is a constant. When taking equal radius particles per unit weight, the specific surface area (S) is:

$$S = 4\pi r^2 / \frac{4}{3}\pi r^3 \rho = 3/\rho r \quad (13)$$

Combining Eq. (12) and Eq. (13), we can get:

$$S = 3k^{\frac{1}{2}} / \rho \alpha^{\frac{1}{2}} \quad (14)$$

Therefore, the smaller the particle size, the larger the specific surface area, which is conducive to improve the reaction rate constant. In this experiment, the particle size of zircon is less than 75 μm, thus significantly reducing the decomposition temperature of zircon and the formation temperature of mullite.

In the sintering process, zircon is decomposed into ZrO_2 and amorphous SiO_2 according to TEM results in Fig. 7. Amorphous SiO_2 dissolves into Al_2O_3 and then reacts with Al_2O_3 to form mullite. Unreacted Al_2O_3 particles still dispersed in the matrix. The reaction between SiO_2 and Al_2O_3 could be divided into three steps: Al ions in Al_2O_3 particles migrate to amorphous SiO_2 phase; Al ions diffuse to the growing mullite grains; Al_2O_3 and mullite are combined into mullite lattice.

The nucleation of amorphous mullite is directly from the amorphous silicate matrix. Mullite nucleation activation energy can be calculated as follows:

$$\gamma = \gamma_0 \exp\left(\frac{E_a}{RT}\right) \quad (15)$$

where γ_0 is the constant, E_a is the crystallization activation energy, and R is the gas constant ($8.31\ J \cdot mol^{-1}$). The higher the sintering temperature, the shorter the nucleation time of mullite.

The activation energy of mullite growth can be calculated by the following equations:

$$a = \exp\left[-\left(k\left(t - \tau\right)\right)^n\right] \quad (16)$$

$$k = k_0 \exp\left(\frac{-E_a}{RT}\right) \quad (17)$$

where a is the volume fraction of mullite (vol.%), t is the sintering time (s), n is the reaction order, and k_0 is a constant. According to the above equations, the higher the temperature and the longer the sintering time, the larger the volume fraction of mullite and the reaction rate coefficient k. With high melting point and good creep resistance, the mullite formed at high temperatures significantly enhances the high temperature flexural strength of Al_2O_3 ceramic cores. In addition, the whisker or columnar structure of mullite can effectively disperse stress and improve the mechanical properties of the material at room temperature.

Figure 8 shows the decomposition behavior of zircon in Al_2O_3 ceramic samples. Zircon is distributed between Al_2O_3 particles, which hinders the migration of Al_2O_3 particles, resulting in a large number of pores between ceramic particles. After sintering, due to the incomplete decomposition of zircon, small-sized SiO_2 and ZrO_2 particles appear around the zircon. [Fig. 8(b)]. ZrO_2 particles migrate to Al_2O_3 particles and are encapsulated in viscous flowing SiO_2 [Fig. 8(c)]. As shown in Figs. 8(d, e), the decomposition of zircon and the viscous flow of SiO_2 promote the sintering of ceramic particles and increase the shrinkage of X and Y axes.

Figure 9 shows the crack propagation behavior in the ceramic core samples after the three-point bending test. The fracture surface of the ceramic core samples is irregular, and there is no obvious cracking within the ceramic particles,

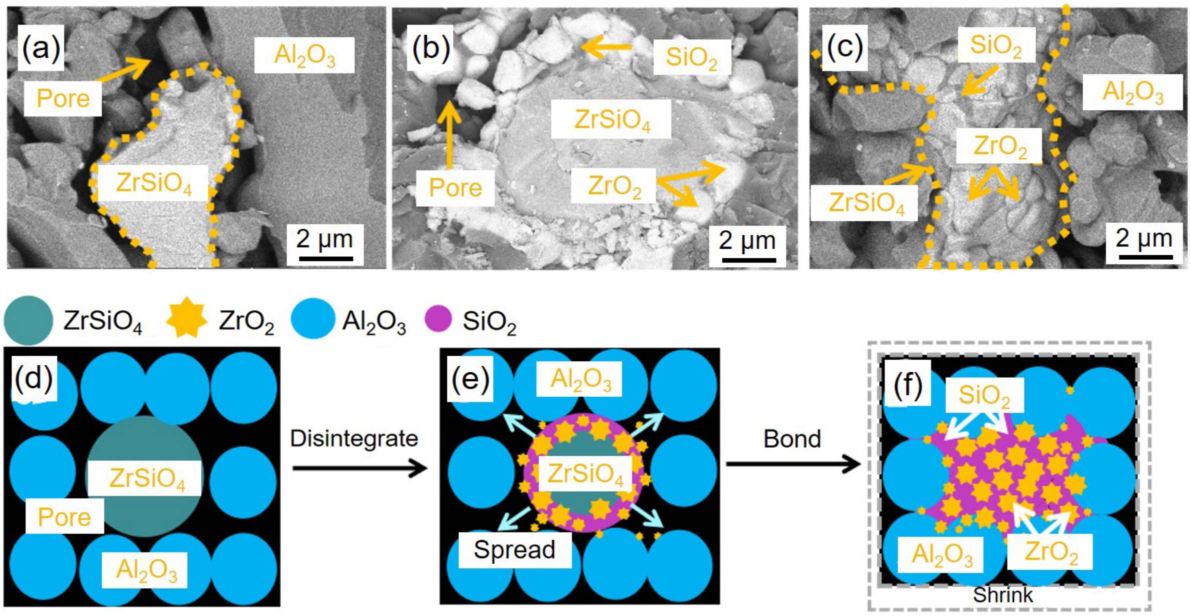

Fig. 8: Schematic diagram of zircon decomposition (a–f)

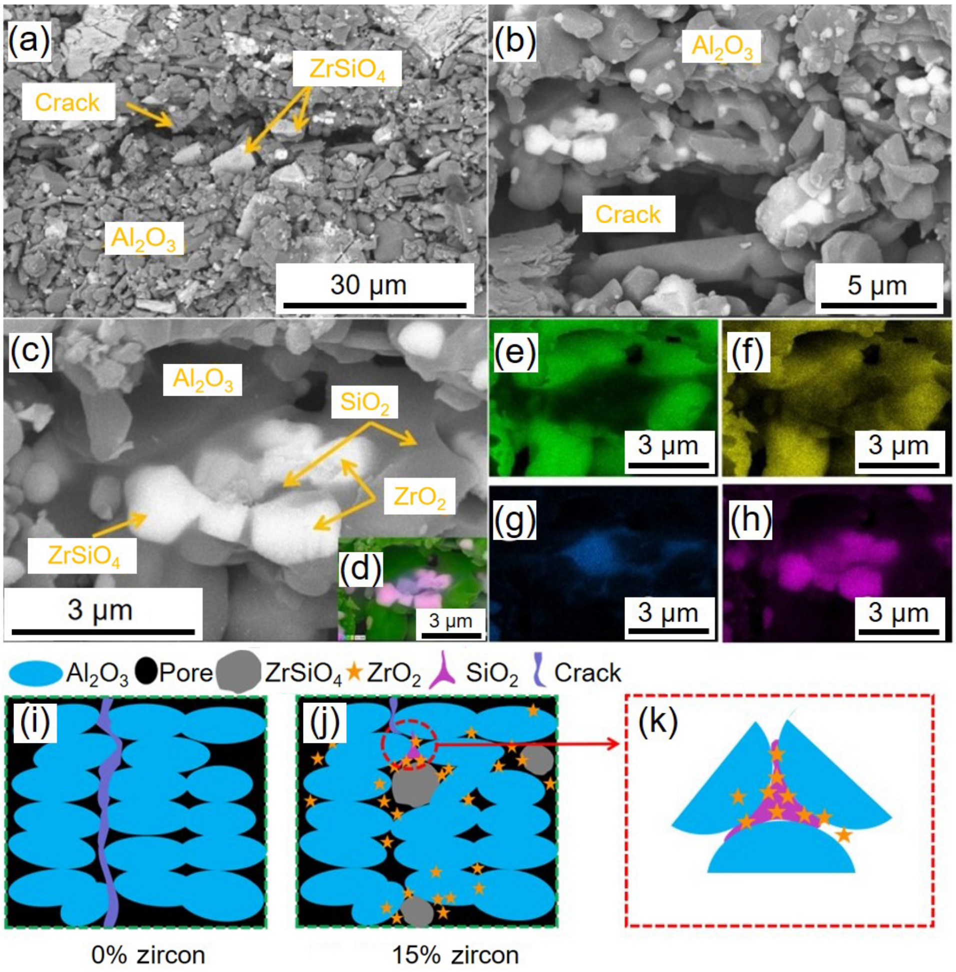

Fig. 9: SEM images (a–c) and element distribution images (d–h) of nano particle reinforced Al_2O_3-based ceramic samples, and schematic diagram showing cracking propagation behavior (i–k)

which proves that the cracks mainly propagate along the interface between the two particles [Figs. 9(a, b)]. In Fig. 9(c), ZrO_2 particles adhere to the surface of Al_2O_3 particles formed by the decomposition of zircon particles. Meanwhile, SiO_2 is filled between Al_2O_3 particles and ZrO_2 particles as a binder. Figures 9(i–k) are a schematic diagram of crack propagation behavior in ceramic samples. The strength of pure Al_2O_3 ceramic cores mainly depends on inter-particle sintering, which leads to the easy expansion of cracks. After adding zircon to the samples, the ZrO_2 and SiO_2 formed by the partial decomposition of zircon promote the bonding between ceramic particles, thereby hindering crack propagation and enhancing the strength.

3.4 Formation and strengthening mechanism of composite layered interface

Figure 10 shows the influence of zircon on the interface of Al_2O_3 ceramic samples. The decomposition of zircon is accompanied by the diffusion and migration of Si to Al_2O_3, and viscous flow in the pores of ceramic particles, which reduces the porosity of core and hinders crack propagation [Fig. 10(b)]. The accumulation state of zircon and Al_2O_3 particles in ceramic samples is shown in Fig. 10(c). ZrO_2 precipitated from zircon is distributed between Al_2O_3 particles and zircon particles as a stable phase at high temperatures and migrate to the pores of ceramic particles which hinder the shrinkage of lamella. As an unstable phase, SiO_2 diffuses from zircon to Al_2O_3 particles, and part of SiO_2 fills between ceramic particles by viscous flow, which promotes the sintering of ceramic particles at the interface and weakens the delamination phenomenon of the ceramic cores, therefore improves the mechanical properties.

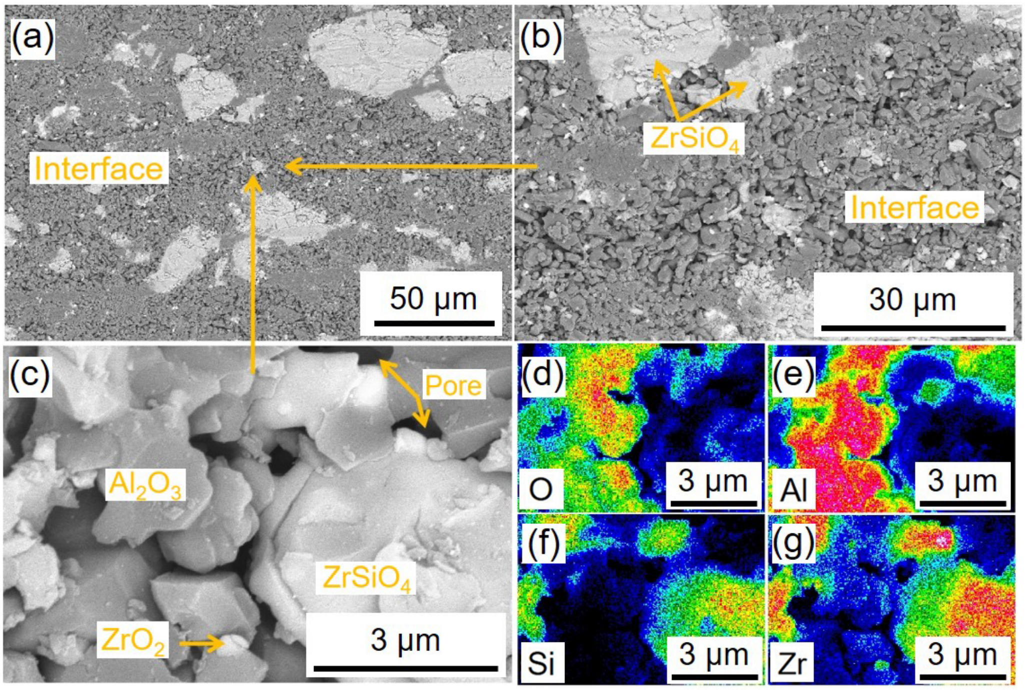

Fig. 10: SEM images (a–c) and element distribution images (d–g) of ceramic cores

4 Conclusions

In this study, Al_2O_3 ceramic cores with different zircon contents were prepared by vat photopolymerization 3D printing technology, and the influence of zircon content on Al_2O_3 ceramic cores was studied. The results are as follows:

(1) As the zircon content increases from 5vol.% to 20vol.%, the sintering shrinkage of ceramic samples along the X and Y axes generally exhibits an upward trend, whereas the Z-axis shrinkage shows an overall downward trend. The open porosity of the ceramic samples exhibits an overall decreasing trend while the bulk density shows a corresponding gradual increase.

(2) When the zircon content is 15vol.%, the Al_2O_3 ceramic core sample demonstrates optimal comprehensive performance. At this time, the porosity of ceramic core samples is 30.75%, the flexural strength is 61.54 MPa at 25 °C, 11.59 MPa at 1,500 °C, and the bulk density is 2.69 $g\cdot cm^{-3}$.

(3) At 1,400 °C, zircon decomposes to form ZrO_2 and SiO_2 phases, weakening the interface delamination of the vat photopolymerization 3D printed Al_2O_3 ceramic core.

(4) This study solves the problems of weak mechanical properties and sintering anisotropy in vat photopolymerization Al_2O_3-based ceramic cores. It is expected these results can establish a theoretical foundation for the application of vat photopolymerization-fabricated Al_2O_3-based ceramic cores with complex structure in the aviation field.

Acknowledgments

This work was financially supported by the National Natural Science Foundation of China (Nos. 52402094, U234120139, and U22A20129), the National Defense Basic Scientific Research Program of China (No. JCKY2022130C005), the China Postdoctoral Science Foundation (No. 2023M743571), the Postdoctoral Fellowship Program of CPSF (No. GZC20232743), the Innovation Project of IMR (2024-PY11), the Open Research Fund of National Key Laboratory of Advanced Casting Technologies (No. CAT2023-006), the Graduate Education Quality Engineering Project of Anhui Province (No. 2023cxcysj015), the Science and Technology Plan Project of

Liaoning Province (No. 2024JH2/101900011), the National Key Research and Development Program of China (Nos. 2024YFB3714500 and 2018YFB1106600), and the China United Gas Turbine Technology Co., Ltd. under the project of J790.

Conflict of interest

The authors declare that they have no known competing financial interests or personal relationships that could have appeared to influence the work reported in this paper. The work described was original research that has not been published previously, and not under consideration for publication elsewhere, in whole or in part. All the authors listed have approved the manuscript that is enclosed.

References

[1] Padture N P, Gell M, Jordan E H, et al. Thermal barrier coatings for gas-turbine engine applications. Science, 2002, 296: 280–284. https://doi.org/10.1126/science.1068609.

[2] Li Q L, Liang J J, Zhang Y L, et al. Fused silica ceramic core based on network-structured zircon design via 3D printing. Scripta Materialia, 2022, 208: 114342. https://doi.org/10.1016/j.scriptamat.2021.114342.

[3] Liang J J, Lin Q H, Zhang X, et al. Effects of alumina on cristobalite crystallization and properties of silica-based ceramic cores. Journal of Materials Science and Technology, 2017, 33: 204–209. https://doi.org/10.1016/j.jmst.2016.02.012.

[4] Bae C J, Kim D, Halloran J W, et al. Mechanical and kinetic studies on the refractory fused silica of integrally cored ceramic mold fabricated by additive manufacturing. Journal of the European Ceramic Society, 2019, 39: 618–623. https://doi.org/10.1016/j.jeurceramsoc.2018.09.013.

[5] Lu Z L, Cao J W, Jing H, et al. Review of main manufacturing processes of complex hollow turbine blades: This paper critically reviews conventional and advanced technologies used for manufacturing hollow turbine blades. Virtual and Physical Prototyping, 2013, 8: 87–95. https://doi.org/10.1080/17452759.2013.790600.

[6] Vecchio C D, Fenu G, Pellegrino F A, et al. Support vector representation machine for superalloy investment casting optimization. Applied Mathematical Modelling, 2019, 72: 324–336. https://doi.org/10.1016/j.apm.2019.02.033.

[7] Kazemi A, Faghihi-Sani M A, Nayyeri M J, et al. Effect of zircon content on chemical and mechanical behavior of silica-based ceramic cores. Ceramics International, 2014, 40: 1093–1098. https://doi.org/10.1016/j.ceramint.2013.06.108.

[8] Lu Z L, Tian G Q, Wan W J, et al. Effect of in situ synthesised mullite whiskers on the high-temperature strength of Al_2O_3-based ceramic moulds for casting hollow turbine blades. Ceramics International, 2016, 42: 18851–18858. https://doi.org/10.1016/j.ceramint.2016.09.031.

[9] Chen Z W, Li Z Y, Li J J, et al. 3D printing of ceramics: A review. Journal of the European Ceramic Society, 2019, 39: 661–687. https://doi.org/10.1016/j.jeurceramsoc.2018.11.013.

[10] Li J G, An X L, Liang J J, et al. Recent advances in the stereolithographic three-dimensional printing of ceramic cores: Challenges and prospects. Journal of Materials Science and Technology, 2022, 117: 79–98. https://doi.org/10.1016/j.jmst.2021.10.041.

[11] Wang L G, Zuo B, Zhu G Z, et al. Effect of roasting process on the properties of alumina-based ceramic core. Advanced Materials Research, 2012, 535–537: 809–813. https://doi.org/10.4028/www.scientific.net/AMR.535-537.809.

[12] Wang L G, Zuo B, Zhu G Z, et al. Effect of SiO_2 micro-powders on the properties of alumina-based ceramic core. Advanced Materials Research, 2012, 554–556: 731–735. https://doi.org/10.4028/www.scientific.net/AMR.554–556.731.

[13] Liu X F, Guo X, Shui G Y, et al. Properties of alumina-based ceramic cores. China Foundry, 2021, 18(6): 593–598. https://doi.org/10.1007/s41230-021-1125-4.

[14] Fan J X, Xu X Q, Niu S X, et al. Anisotropy management on microstructure and mechanical property in 3D printing of silica-based ceramic cores. Journal of the European Ceramic Society, 2022, 42: 4388–4395. https://doi.org/10.1016/j.jeurceramsoc.2022.03.059.

[15] Qiu Y X, Li Q L, Yang K, et al. Thermal shock resistant 3D printed ceramics reinforced with $MgAl_2O_4$ shell structure. Journal of Materials Science and Technology, 2024, 178: 100–111. https://doi.org/10.1016/j.jmst.2023.09.004.

[16] Dong W J, Li Q L, Chen T C, et al. Effect of sintering temperature on microstructure and properties of 3D printing polysilazane reinforced Al_2O_3 core. China Foundry, 2023, 20(5): 387–394. https://doi.org/10.1007/s41230-023-2122-6.

[17] Seo J W, Kim G M, Choi Y, et al. Improving printability of digital-light-processing 3D bioprinting via photoabsorber pigment adjustment. International Journal of Molecular Sciences, 2022, 23: 5428. https://doi.org/10.3390/ijms23105428.

[18] Luo J Q, Liu B, Huang W J, et al. The preparation of zirconia slurry based on DLP additive manufacturing technology. Journal of the Australian Ceramic Society, 2022, 58: 1015–1023. https://doi.org/10.1007/s41779-022-00758-7.

[19] Hu K H, Wang H Y, Lu K, et al. Fabrication of silica-based ceramic cores with internal lattice structures by stereolithography. China Foundry, 2022, 19(5): 369–379. https://doi.org/10.1007/s41230-022-2048-4.

[20] Lu X Y, Liu G, Lu J. Development of ceramic 3D/4D printing in China. Additive Manufacturing Frontiers, 2024, 3: 200158. https://doi.org/10.1016/j.amf.2024.200158.

[21] Li H, Liu Y S, Liu Y S, et al. Evolution of the microstructure and mechanical properties of stereolithography formed alumina cores sintered in vacuum. Journal of the European Ceramic Society, 2020, 40: 4825–4836. https://doi.org/10.1016/j.jeurceramsoc.2019.11.047.

[22] Yang Z, Zhao Z, Yu J, et al. Effect of silicone resin as precursor and binder on the properties of alumina-based ceramic cores using ball-shaped powders. Ceramics International, 2019, 45: 2170–2177. https://doi.org/10.1016/j.ceramint.2018.10.127.

[23] Li Q L, An X L, Liang J J, et al. Balancing flexural strength and porosity in DLP-3D printing Al_2O_3 cores for hollow turbine blades. Journal of Materials Science & Technology, 2022, 104: 19–32.

[24] Wang R F, Zhang D M, Zhuang O Y, et al. Effect of Y_2O_3 content on the properties of alumina-based ceramic cores. Applied Mechanics and Materials, 2014, 488: 145–149. https://doi.org/10.4028/www.scientific.net/AMM.488-489.145.

[25] Li Q L, Li J G, Liang J J, et al. Research progress in ceramic core of hollow blades by photocurable 3D printing. Special Casting and Nonferrous Alloys, 2021, 41: 1339–1344. (In Chinese)

[26] Li H, Liu Y S, Colombo P, et al. The influence of sintering procedure and porosity on the properties of 3D printed alumina ceramic cores. Ceramics International, 2021, 47: 27668–27676. https://doi.org/10.1016/j.ceramint.2021.06.191.

[27] Griffith M L, Halloran J W. Freeform fabrication of ceramics via stereolithography. Journal of the American Ceramic Society, 1996, 79: 2601–2608. https://doi.org/10.1111/j.1151-2916.1996.tb09022.x.

[28] Wilson P J, Blackburn S, Greenwood R W, et al. The role of zircon particle size distribution, surface area and contamination on the properties of silica-zircon ceramic materials. Journal of the European Ceramic Society, 2011, 31: 1849–1855. https://doi.org/10.1016/j.jeurceramsoc.2011.03.005.

[29] Ren Q, Liu C X, Zhang Q, et al. Effects of B_2O_3 substitution for Al_2O_3 on the crystallization and properties of translucent mica glass-ceramics. Journal of the European Ceramic Society, 2021, 41: 334–341. https://doi.org/10.1016/j.jeurceramsoc.2021.09.048.

[30] Zhao D, Su H J, Hu K H, et al. Formation mechanism and controlling strategy of lamellar structure in 3D printed alumina ceramics by digital light processing. Additive Manufacturing, 2022, 52: 102650. https://doi.org/10.1016/j.addma.2022.102650.

[31] Pan Z P, Guo J Z, Li S M, et al. Effect of nonuniform sintering on mechanical and thermal properties of silica-based ceramic cores. China Foundry, 2021, 18(5): 457–462. https://doi.org/10.1007/s41230-021-1024-8.

[32] Zhang J, Yu K B, Wu J M, et al. Effects of $ZrSiO_4$ content on properties of SiO_2-based ceramics prepared by digital light processing. Ceramics International, 2023, 49(6): 9584–9591. https://doi.org/10.1016/j.ceramint.2022.11.128.

[33] Li Q L, Meng X T, Zhang X C, et al. Enhanced 3D printed Al_2O_3 core via in-situ mullite. Additive Manufacturing, 2022, 55: 102826. https://doi.org/10.1016/j.addma.2022.102826.

[34] Huo M D, Li Q L, Liu J Q, et al. In-situ synthesis of high-performance Al_2O_3-based ceramic cores reinforced with core-shell structures. Ceramics International, 2022, 48: 33693–33703. https://doi.org/10.1016/j.ceramint.2022.07.315.

[35] Liu J Q, Li Q L, Huo M D, et al. Microstructure and mechanical properties of 3D-printed nano-silica reinforced alumina cores. Ceramics International, 2022, 48: 30282–30293. https://doi.org/10.1016/j.ceramint.2022.06.301.

[36] Davis R F, Aksay I A, Pask J A. Decomposition of mullite. Journal of the American Ceramic Society, 1972, 55(2): 98–101. https://doi.org/10.1111/j.1151-2916.1972.tb11218.x.

[37] Mathias P M. The Gibbs-Helmholtz equation in chemical process technology, Industrial and Engineering Chemistry Research, 2016, 55: 1076–1087. https://doi.org/10.1021/acs.iecr.5b03405.

[38] Robie R A, Hemingway B S, Fisher J R. Thermodynamic properties of minerals and related substances at 298.15 K and 1 bar (105 pascals) pressure and at higher temperatures. Department of the Interior, US Geological Survey, 1978.

[39] Li Y T, Yang J. Research progress of low-temperature sintering additives of alumina ceramics. Bulletin of the Chinese Ceramic Society, 2011, 30: 1328–1332.

[40] Cho K H, Jang H, Hong Y S, et al. The size effect of zircon particles on the friction characteristics of brake lining materials. Wear, 2008, 264: 291–297. https://doi.org/10.1016/j.wear.2007.03.018.